



Development of heteroatom-rich fluorene-based benzoxazine-linked porous organic polymers as potential candidates for energy storage

Ahmed F. Saber^a, Ahmed F.M. EL-Mahdy^{b,*}, Shiao-Wei Kuo^{b,*}

^a Interdisciplinary Research Center for Hydrogen Technologies and Carbon Management (IRCHTCM), King Fahd University of Petroleum & Minerals, Dhahran 31261, Saudi Arabia

^b Department of Materials and Optoelectronic Science, National Sun Yat-Sen University, Kaohsiung 80424, Taiwan

ARTICLE INFO

Keywords:

Porous organic polymers
Benzoxazine-based
Heteroatom-rich
Supercapacitors

ABSTRACT

Background: Engineering of porous organic polymers (POPs) with redox activity, considerable porosity, and high conductivity is more crucial for their practical applications in energy storage systems.

Methods: In this context, we describe the synthesis and comprehensive characterization of two novel fluorene-based benzoxazine-linked POPs as efficient electrode materials for supercapacitors. The polymers have been obtained in high yields by direct polymerization of different triamine derivatives, diphenol and *p*-formaldehyde. The structural integrity of the benzoxazine-based polymer linkage and porosity parameters have been readily investigated through FTIR, solid-state ¹³C NMR spectra and N₂ sorption analysis. The benzoxazine backbone endows the POPs with abundant N and O heteroatoms, making them efficient candidates for storing energy.

Significant Findings: We have found that the benzoxazine-linked polymers exhibit outstanding electrochemical specific capacitances. Of the two polymers synthesized investigated, FI-TPA POP displayed higher electrochemical specific capacitance of up to 276 F g⁻¹ at 0.5 A g⁻¹ than FI-Cz POP, which is attributed to the higher microporosity and the larger specific surface area. Furthermore, FI-TPA POP exhibited the maximum energy density of 38.33 Wh kg⁻¹ at a power density of 250 W kg⁻¹, top cyclic stability after 5000 charge-discharge cycles (95.23 %) and the lowest ohmic internal resistance (21.83 Ω).

1. Introduction

Over the past decade, there has been remarkable progress and heightened attention on sustainable energy sources, driven by growing concerns about environmental pollution, climate change, and the urgent need to address energy security. These challenges have prompted considerable efforts to discover novel alternatives for energy storage to meet future energy demands [1–5]. Consequently, there has been an increasing emphasis on wind energy management and renewable energy conversion. However, several obstacles, including low energy density, lack of structural integrity, and limited lifespan, hinder the implementation of energy storage devices. Alternatively, advanced energy storage systems are crucial owing to their enhanced energy efficiency, rapid energy absorption, and support for the evolution of renewable energy sources [6,7]. The current energy crisis has intensified the focus on innovative technologies, particularly energy storage solutions [8]. Recently, substantial research has been dedicated to developing energy storage technologies from renewable sources and utilizing them as

needed [9–11]. These technologies are essential for keeping pace with rapid advancements in sectors that require high power and energy densities, such as portable electronics and electric vehicles. Supercapacitors (SCs) are considered one of the most promising devices for electrochemical energy storage. SCs have the potential to replace traditional capacitors and batteries, offering key advantages for sustainable energy storage [12,13]. Among their many advantages, SCs are known for their safety, exceptional electrochemical performance, long cycle life, and environmental sustainability [14–16]. SCs hold notable value in various applications owing to their fast charge–discharge capabilities, extended service life, and excellent operational performance.

Porous organic polymers (POPs) represent multidimensional network materials characterized by intrinsic porosity and composed of various geometric and topological organic monomers interconnected by robust covalent bonds [17–19]. Recently, POPs have attracted considerable attention as a rapidly evolving research domain within the field of porous materials [20]. POPs can be classified into two primary categories based on their degree of order: amorphous polymers, which

* Corresponding authors.

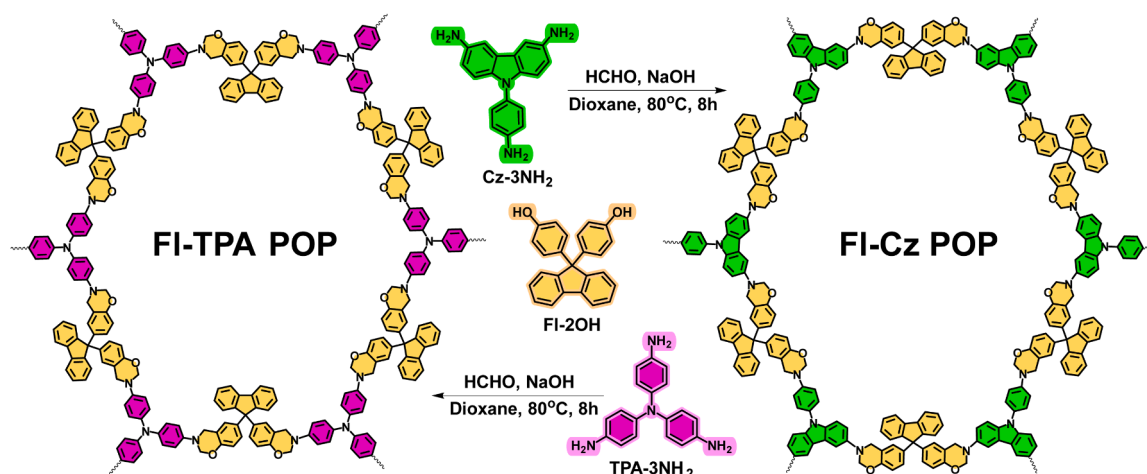
E-mail addresses: ahmedelmahdy@mail.nsysu.edu.tw (A.F.M. EL-Mahdy), kuosw@faculty.nsysu.edu.tw (S.-W. Kuo).

<https://doi.org/10.1016/j.jtice.2024.105935>

Received 28 July 2024; Received in revised form 6 December 2024; Accepted 24 December 2024

Available online 29 December 2024

1876-1070/© 2024 Taiwan Institute of Chemical Engineers. Published by Elsevier B.V. All rights are reserved, including those for text and data mining, AI training, and similar technologies.



Scheme 1. Preparation of (a) FI-TPA and (b) FI-Cz POPs.

include porous aromatic frameworks (PAFs), conjugated microporous polymers (CMPs), and hyper-crosslinked polymers (HCPs), and crystalline polymers, exemplified by covalent organic frameworks (COFs) [21, 22]. Furthermore, based on their porosity, POPs can be categorized into macroporous (with pore sizes exceeding 50 nm), mesoporous (2–50 nm), and microporous (<2 nm) materials [23]. The lightweight nature, substantial porosity, high physicochemical stability, customizable structures, and ease of modification of POPs have generated considerable interest in both research and practical applications [24–29]. The synthesized POP materials have demonstrated diverse applications in gas capture and separation, photoelectric conversion, photocatalysis, supercapacitors, and biomedical fields such as drug delivery and biosensing [30–33]. Notably, POPs have emerged as exceptional electrode materials for SCs owing to their cost-effectiveness, large specific surface areas, tunable pore sizes, and high stability [34].

Heteroatom-rich POPs are noteworthy organic materials that have garnered substantial interest due to their applications in energy storage and various other fields [35,36]. In particular, N-rich polymeric materials exhibit inherent photoelectric properties, which have attracted considerable attention from researchers [37]. For instance, polymeric structures with a high nitrogen heteroatom content have demonstrated not only increased conductivity but also enhanced wettability, which contributes significantly to pseudo-capacitance and results in superior electrochemical performance [38,39].

Benzoxazine-linked materials (BZ) are a fascinating class of heteroatom-rich compounds synthesized through the condensation reaction of phenol, amine, and formaldehyde. These materials exhibit outstanding electronic, thermal, and mechanical properties, along with excellent stability [40–44]. The oxazine ring contains nitrogen and oxygen heteroatoms distributed above and below the ring, adopting a deformed half-chair conformation that imparts a degree of rigidity [45]. Consequently, the BZ building unit provides significant amounts of nitrogen and oxygen heteroatoms to the polymers. In recent years, researchers have focused on synthesizing BZ-based porous materials through ring-opening thermal polymerization or by creating microporous carbons from polybenzoxazine starting materials [46–49]. However, the direct application of BZ linkages for the preparation of POPs has been infrequently achieved [50].

Fluorene-based (FI) derivatives exhibit a range of advantageous properties that render them promising candidates for applications in optoelectronics, membranes, sensors, photomechanical materials, and various other domains within science and technology [51–56]. Fluorenes are notable materials characterized by a rigid planar biphenyl structure and a highly conjugated system [57]. This unique structural unit provides several benefits over other polyaromatic scaffolds, including enhanced solubility, stability, and exceptional photophysical

properties. A key advantage of the FI ring is its capacity for facile substitution with diverse aromatic or heterocyclic fragments, which facilitates modifications of its electronic properties and broadens its applicability [58]. Consequently, numerous FI-based polymeric materials have been designed and synthesized over the past few decades.

Based on the information presented, two novel FI-based BZ-linked POPs were synthesized using different triamine monomers, which were condensed with paraformaldehyde and 4,4'-(9H-fluorene-9,9-diyl)diphenol via Mannich condensation (Scheme 1). Unlike conventional BZ polymeric resins, typically obtained through thermal polymerization and ring-opening of BZ rings within polymer chains, the POPs synthesized in our research consist of extended oxazine units without undergoing a ring-opening process [59,60]. The BZ-linked POPs, named FI-TPA and FI-Cz, were synthesized through the polymerization reaction of 4,4'-(9H-fluorene-9,9-diyl)diphenol (FI-2OH) and paraformaldehyde with tris(4-aminophenyl)amine (TPA-3NH₂) and 9-(4-aminophenyl)-9H-carbazole-3,6-diamine (Cz-3NH₂), respectively. The FI-TPA and FI-Cz POPs were obtained as insoluble solid materials with yields of 88.46 % and 84.57 %, respectively. The porosity of the materials was characterized using N₂ sorption isotherms, which confirmed the polymers' porous structure, with pore sizes predominantly the microporous range. The potential of the synthesized BZ-based POPs as efficient electrodes for SCs has been evaluated through electrochemical measurements, yielding a specific capacitance of up to 276 F g⁻¹ and an energy density of up to 38.33 Wh kg⁻¹.

2. Experimental section

2.1. Materials and characterizations

All chemicals were obtained from commercial suppliers and used as received, unless otherwise noted. 4,4'-(9H-fluorene-9,9-diyl)diphenol (FI-2OH), paraformaldehyde (HCHO), sodium hydroxide (NaOH), acetic acid (99.8 %), copper(II) nitrate trihydrate (98 %), acetic anhydride (99 %), and carbazole (>95 %) were sourced from Sigma-Aldrich. Palladium on activated carbon (10 % Pd/C) was obtained from Acros, while hydrazine monohydrate (≥98 %), 1-fluoro-4-nitrobenzene (99 %), and potassium carbonate (K₂CO₃, 99.9 %) were procured from Alfa Aesar. 1,4-Dioxane and dimethyl sulfoxide (DMSO) were purchased from J.T. Baker. 4-Nitroaniline (99 %) was acquired from Fluka, and ethanol (EtOH) was ordered from Kelong Chemistry Reagent. All characterizations of the prepared BZ-linked polymers are presented in the Supporting Information (ESI).

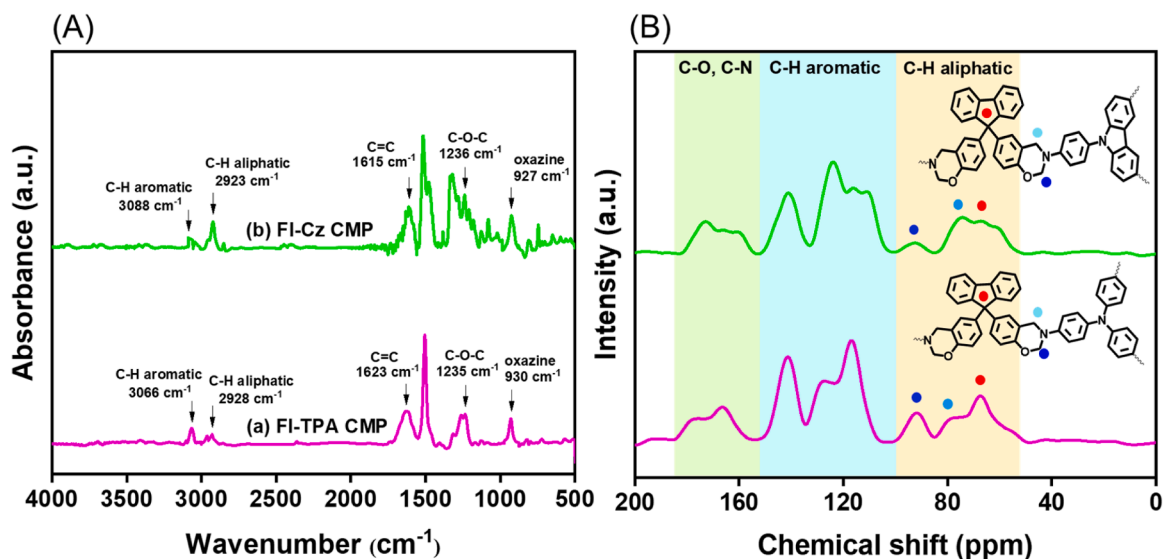


Fig. 1. (A) FTIR spectroscopy; and (B) SS ¹³C NMR spectroscopy of FI-TPA and FI-Cz POPs.

2.2. Preparations of POPs

A solution of 3.3 mmol of the triamines (TPA-3NH₂, Cz-3NH₂) in dioxane was gradually added to a suspension of 40 mmol HCHO in dioxane, along with two drops of 1 M NaOH, while maintaining a temperature of 5 °C–10 °C. The resulting suspension was stirred for 2 h

prior to the addition of 10 mmol of FI-2OH in dioxane. The mixture was subsequently stirred at 80 °C for an additional 8 h. The resulting powder was filtered and extensively washed to yield the corresponding FI-based POPs. Finally, the obtained precipitate was dried at 120 °C for 10 h under vacuum. The complete synthetic procedures are detailed in the (ESI).

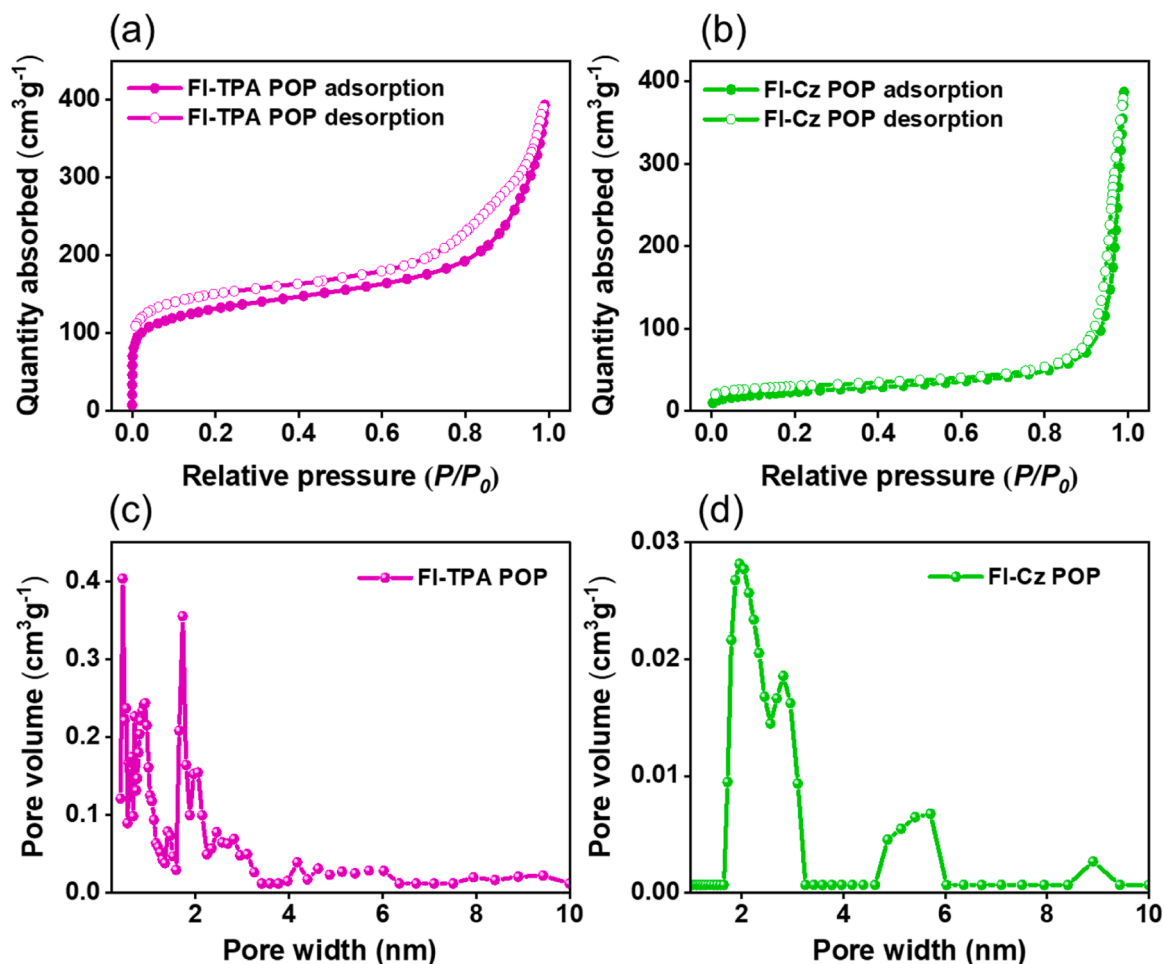


Fig. 2. Nitrogen sorption curves of (a,b) FI-TPA and FI-Cz polymers and the pore size distribution profiles of (c,d) FI-TPA and FI-Cz POPs.

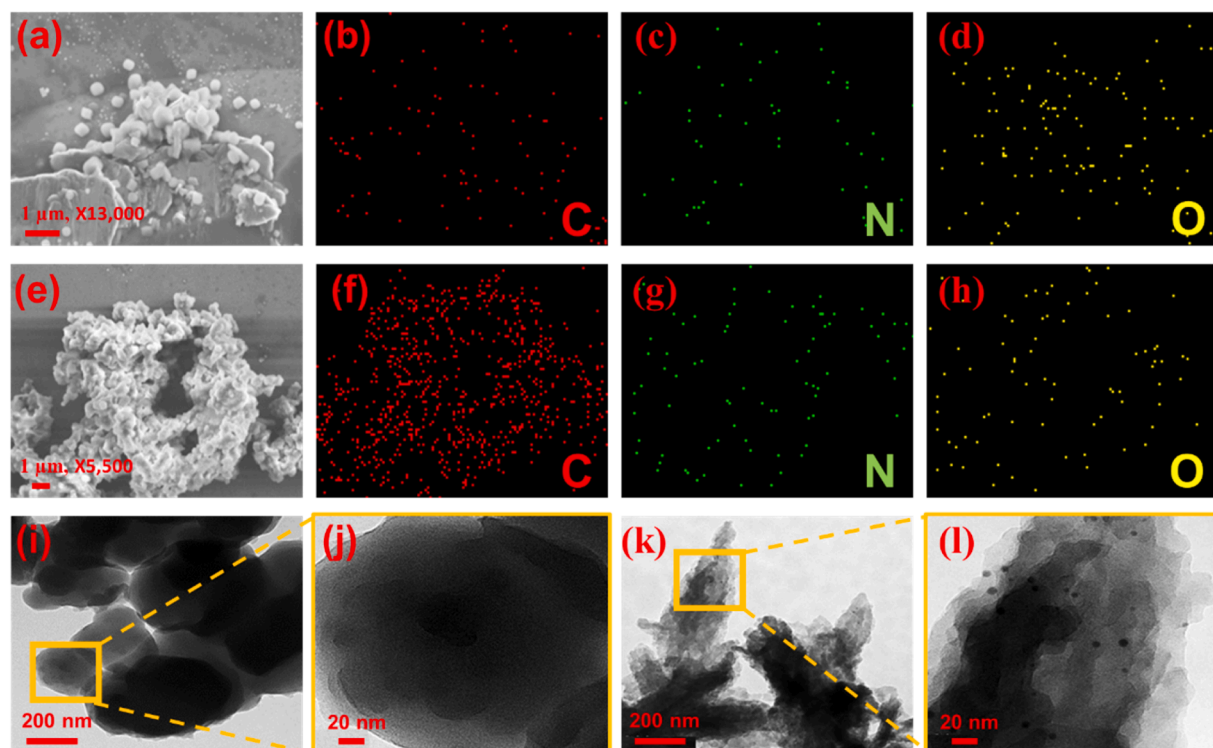


Fig. 3. SEM images of (a) FI-TPA and (e) FI-Cz POPs. EDX images of (b–d) FI-TPA and (f–h) FI-Cz polymers. TEM images of (i) FI-TPA and (k) FI-Cz POPs. HR-TEM images of (j) FI-TPA and (l) FI-Cz polymers.

3. Results and discussion

3.1. Structural design, preparation, and characterization

Scheme 1 illustrates the construction of FI-based BZ-linked polymers utilizing the one-pot Mannich coupling reaction. The successful polymerization was confirmed through Fourier transform infrared spectroscopy (FTIR) and solid-state ^{13}C nuclear magnetic resonance (SS ^{13}C NMR). First, as depicted in Fig. 1A and Figures S10 and S11, the FI-TPA polymer exhibited vibrational peaks at 1234 and 1078 cm^{-1} , indicating the presence of the aromatic ether group in the BZ unit. These peaks correspond to the asymmetric and symmetric C–O–C vibrational modes, respectively [61]. The corresponding peaks for the FI-Cz polymer were observed at 1236 and 1080 cm^{-1} . Notably, the absorption bands at 922 and 927 cm^{-1} are attributed to the vibration of phenyl rings attached to oxazine units in the FI-TPA and FI-Cz polymers, respectively. Furthermore, the stretching vibrational peaks associated with C–H aliphatic and C–H aromatic functionalities for the FI-TPA polymer were noted at 2927 and 3035 cm^{-1} , respectively, while for the FI-Cz polymer, they were observed at 2923 and 3088 cm^{-1} .

In the SS ^{13}C NMR spectra, three distinct regions of peaks were clearly observed. The signals in the range of 52–100 ppm were primarily characteristic of quaternary carbon atoms and methylene carbons directly bonded to oxygen and nitrogen atoms, providing strong evidence for the formation of the oxazine ring. The quaternary carbon atoms were located around 65–70 ppm, followed by benzylic CH_2 carbons around 80 ppm, and N– CH_2 –O carbon nuclei around 90–100 ppm [62,63]. The intense peaks observed in the range of 103–152 ppm are associated with the aromatic carbon atoms. Additionally, the faint peaks within the range of 153–181 ppm are attributed to C–O and C–N carbon nuclei of the as-prepared polymers. (Fig. 1B)

The enhanced thermal stability of the synthesized BZ-linked polymers was evaluated using thermogravimetric analysis (TGA) performed in a nitrogen atmosphere. The TGA results indicated a substantial degree of thermal stability, with the FI-Cz POP demonstrating the highest

thermal stability at 388 $^{\circ}\text{C}$, slightly exceeding that of the FI-TPA POP, which exhibited a thermal stability of 368 $^{\circ}\text{C}$. Additionally, TGA provided char yield values for the FI-TPA and FI-Cz polymers, estimated at 42 % and 69 %, respectively. (Figure S12 and Table S1)

X-ray diffraction (XRD) analysis of our polymers shows no diffraction signals, confirming their amorphous structure (Figure S13), as reported for other POPs in the literature [64,65].

3.2. Porosity and morphology

Porosity investigations were conducted using N_2 sorption at 77 K. The N_2 sorption isotherms revealed a class II isotherm, indicative of microporosity. (Figs. 2a,b) The FI-TPA polymer exhibited the maximum BET surface area (S_{BET}) of 455 $\text{m}^2 \text{g}^{-1}$, while the FI-Cz POP demonstrated the smallest S_{BET} at 92 $\text{m}^2 \text{g}^{-1}$. The pore size distributions of the FI-based polymers were estimated using non-local density functional theory. The calculated pore sizes were primarily distributed within the microporous and mesoporous ranges. The observed mesoporosity can be attributed to the interparticle voids created by the loose packing of small particles. The FI-TPA polymer displayed three micropores with pore widths of 0.44, 0.92, and 1.72 nm, as well as two mesopores at 2.05 and 2.82 nm. In contrast, the FI-Cz POP exhibited one micropore at 1.96 nm along with three mesopores at 2.82, 5.71, and 8.90 nm. Furthermore, the total pore volumes were estimated to be 0.40 and 0.03 $\text{cm}^3 \text{g}^{-1}$ for the major micropores of the FI-TPA and FI-Cz POPs, respectively. (Figs. 2c, d and Table S2). The FI-TPA polymer demonstrated a higher S_{BET} value compared to the FI-Cz POP, which can be explained by the more densely packed structure of the FI-Cz POP resulting from the planar arrangement of the Cz building unit. The particle size of the prepared polymers was analyzed using Dynamic Light Scattering. As depicted in Figure S14, the dispersed aqueous solution of the FI-TPA polymer contains irregularly agglomerated large particles, with sizes ranging from 458 to 6096 nm. In comparison, the FI-Cz polymer exhibits particle sizes between 569 and 6024 nm. The presence of these large particles, particularly in the FI-TPA POP, may increase light scattering due to the broad particle size

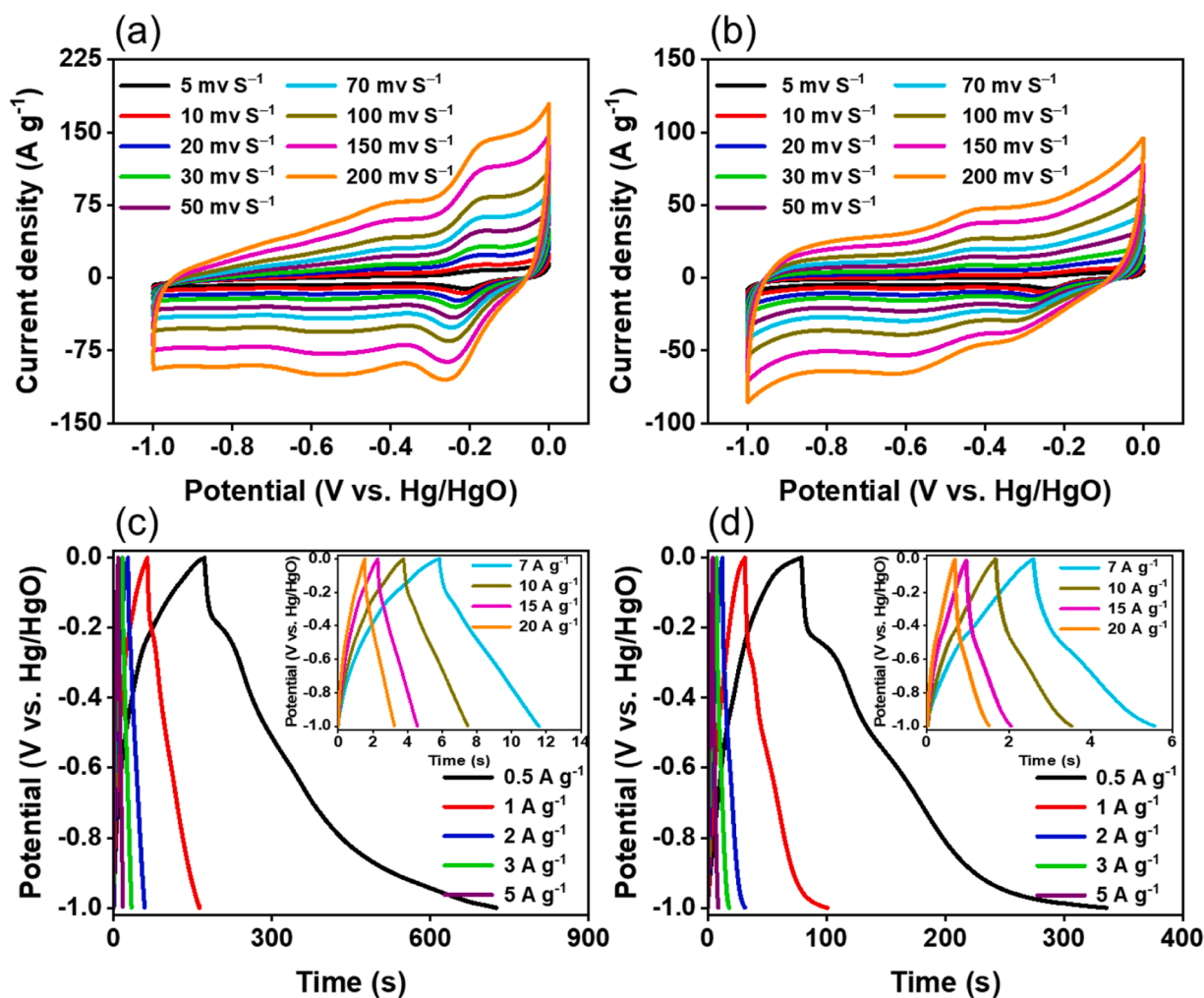


Fig. 4. CV curves of (a) FI-TPA and (b) FI-Cz polymers. GCD curves of (c) FI-TPA and (d) FI-Cz polymers, measured at different current densities.

distribution [66].

The structure and morphology of our novel polymers were examined using both scanning electron microscopy (SEM) and transmission electron microscopy (TEM). The SEM images indicated that the BZ-linked polymers formed accumulated microgel particles with sizes $< 1 \mu\text{m}$. The FI-TPA POP exhibited a spherical morphology, whereas the FI-Cz POP displayed a sponge-like morphology (Figs. 3a,e). Elemental mapping from energy dispersive X-ray spectroscopy revealed a symmetrical distribution of C, N and O atoms on the surface of all polymeric materials (Figs. 3b–d, 3f–h). The TEM and corresponding high-resolution TEM (HR-TEM) images demonstrated an amorphous porous texture for all polymers. (Figures 3i–l)

3.3. Electrochemical measurements

In our pursuit of sustainable energy storage solutions, we have investigated the potential of our synthesized FI-based BZ-linked polymers, focusing on their efficacy as organic electrode materials for SCs. Cyclic voltammetry (CV) measurements were conducted on these polymers using a three-electrode system with a 1.0 M KOH aqueous solution, evaluating their electrochemical behavior over a defined potential range (-1.0 to 0 V). The resulting CV curves exhibited a semi-rectangular shape, with small distinct humps observed within the applied potential window. (Figs. 4a,b) As the scan rate increased, a corresponding rise in the CV peak current was observed for our BZ-linked electrodes. This phenomenon suggests that their electrochemical specific capacitance is influenced by both pseudo-capacitance

and electric double-layer capacitance (EDLC), with minimal charge transfer resistance [67]. The small humps observed in the CV curves are primarily attributed to the presence of N and O heteroatoms, as well as electron-rich phenyl rings. These features also contribute to the enhanced pseudo-capacitance of the materials.

The electrochemical storage properties of SCs are influenced by both EDLC and faradaic redox reactions. In the CV analysis of our FI-based polymers, we observed distinct redox peaks in each case. The FI-TPA POP included a strong redox peak at $-0.29/-0.21$ V, while the FI-Cz POP exhibited this redox peak at $-0.28/-0.23$ V with lower intensity. These redox peaks result from the presence of sufficient redox-active nitrogen and oxygen heteroatoms. Furthermore, the presence of such peaks indicates that redox processes significantly contribute to the capacitance of these polymeric materials. To further clarify this point, the existence of these redox peaks demonstrates that the FI-based POPs undergo reversible redox reactions during the charge–discharge cycles, enhancing their overall capacitance. The specific potentials at which these redox reactions occur suggest that certain functional groups within the FI framework are actively participating in the electrochemical process. This behavior is characteristic of faradaic reactions, where electron transfer occurs between the electrode and the electroactive species in the polymer.

Galvanostatic charge–discharge (GCD) measurements were conducted for all synthesized FI-based POPs over a current density range of 0.5 to 20 A g^{-1} . (Figs. 4c,d) The GCD curves exhibited a triangular shape with minor deflections, indicating the contributions of both EDLC and pseudo-capacitance to the overall electrochemical capacitance. These

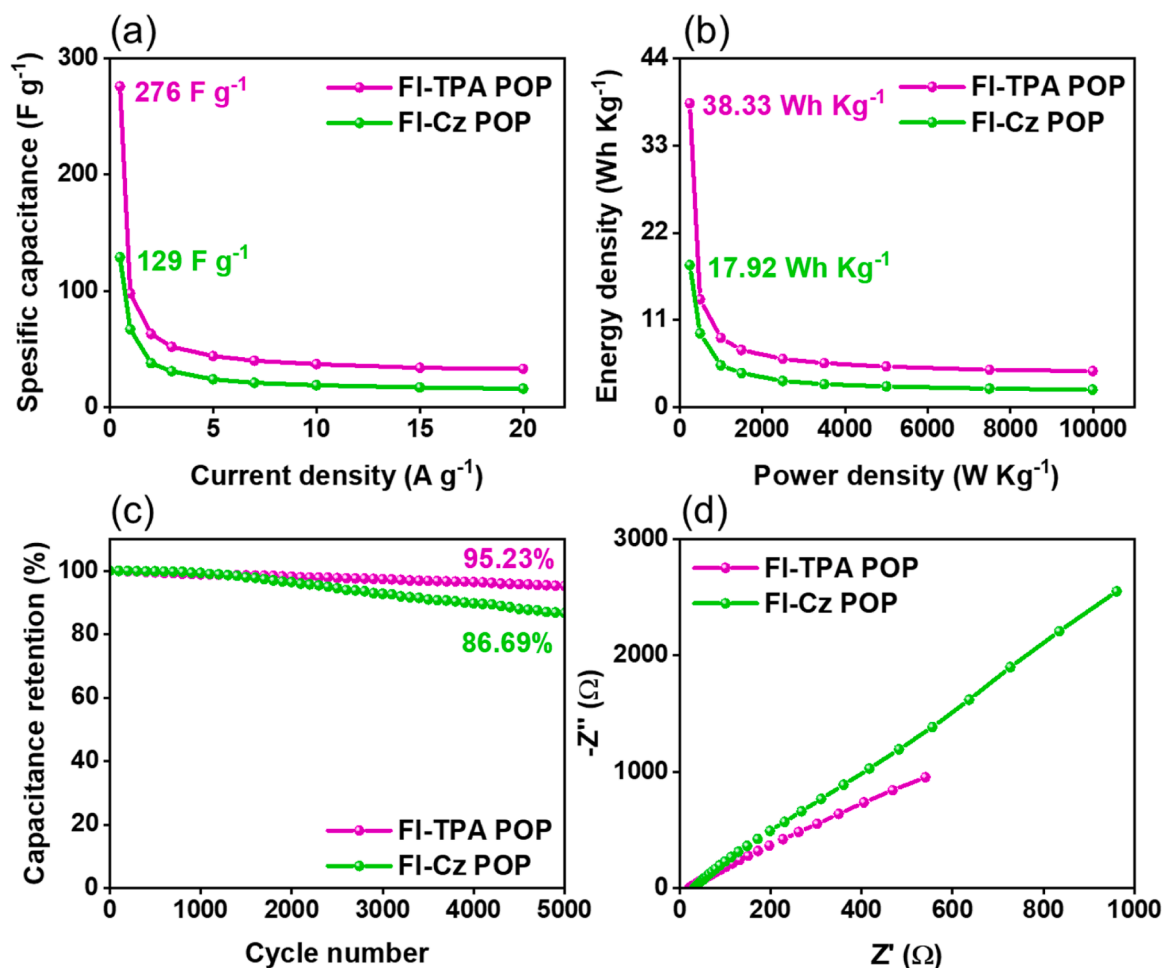


Fig. 5. (a) GCD electrochemical capacitances of FI-TPA and FI-Cz POPs measured at different current densities. (b) Ragone curves. (c) Retention stability. (d) Nyquist curves of the polymeric electrodes.

results are consistent with the findings from the CV analysis. GCD cycles at varying current densities were plotted to determine the actual time for each charge–discharge cycle for both polymers. (Figure S15) The GCD measurements revealed specific capacitances for the FI-TPA polymer of 276, 98, 63, and $52 F g^{-1}$ at current densities of 0.5, 1, 2, and $3 A g^{-1}$, respectively, which align well with the findings from the CV curves. At a current density of $0.5 A g^{-1}$, the higher electrochemical capacitance of the FI-TPA polymer ($276 F g^{-1}$), nearly double that of the FI-Cz polymer ($129 F g^{-1}$), can be attributed to the smaller diffusion rate of KOH ions within the confined pores of the FI-Cz POP. This limitation hinders the ability of ions to effectively reach the polymeric electrode at higher currents. (Fig. 5a) Consequently, increasing the current density results in a notable decrease in ion mobility, which markedly reduces the specific capacitance. Furthermore, Table S3 compares the performance of our BZ-linked POPs with other previously reported electrodes. For example, Mei et al. synthesized MPC-CMPs and subsequently hybridized them with carbon nanotubes (CNTs) using vacuum filtration. Their GCD analysis at $1.0 A g^{-1}$ indicated that the GCD capacitance of CoPc-CMP is $13.8 F g^{-1}$ in $1 M H_2SO_4$ [68]. Additionally, Khattak et al. synthesized DAB-TFP COF and utilized it as electrode material, obtaining an electrochemical capacitance of $98 F g^{-1}$ at a current density of $0.5 A g^{-1}$ [69]. Moreover, the TAPT-DHTA-COF0.05@PPZS900 demonstrated electrochemical capacitances of up to $178 F g^{-1}$ at $1.0 A g^{-1}$ in a $6 M KOH$ aqueous solution [70]. However, the synthesized FI-based POPs surpassed these other electrode materials in terms of electrochemical performance. Furthermore, their synthetic route is straightforward, cost-effective, and scalable for future research.

The Ragone plots of the FI-TPA POP demonstrated an energy density of $38.33 Wh kg^{-1}$ in a three-electrode system at a power density of $250 W kg^{-1}$, while the corresponding energy density for the FI-Cz POP was measured at $17.92 Wh kg^{-1}$. (Fig. 5b) Stability retention measurements are critical for evaluating the Coulombic efficiency and retention capacity of the electrode material. Fig. 5c illustrates the retention stability of the FI-based POP electrodes, which maintained 95.23% and 86.69% of their original capacitance, respectively.

As outlined in Fig. 5d, further electrochemical measurements of the electrode materials are warranted. The Nyquist curve illustrates the resistance spectrum, featuring a straight line in both high and low frequency regions. The first intercept of this curve with the X-axis indicates the solution impedance, which includes intrinsic electrode impedance, ionic KOH resistance, internal electrode resistance, and the impedance between the electrode and KOH electrolyte. Additionally, the slope observed at low frequencies in this curve indicates the diffusion Warburg impedance, which describes the diffusion of both ions and electrons within the electrode, facilitating their transfer. The Nyquist plots reveal that the impedance of the FI-TPA and FI-Cz POPs is 21.83Ω and 32.13Ω , respectively, indicating lower impedance and thereby greater electrochemical capacitance of the as-synthesized polymeric electrodes.

The excellent capacitive behavior of our POPs was further validated by frequency-dependent magnitude Bode plots, which displayed negative slopes at lower frequencies and minimal impedance at higher frequency ranges. (Figure S16a) The knee frequency, defined as the point at a 45° phase angle where capacitance and resistance properties are equivalent, was determined using frequency-dependent phase-angle

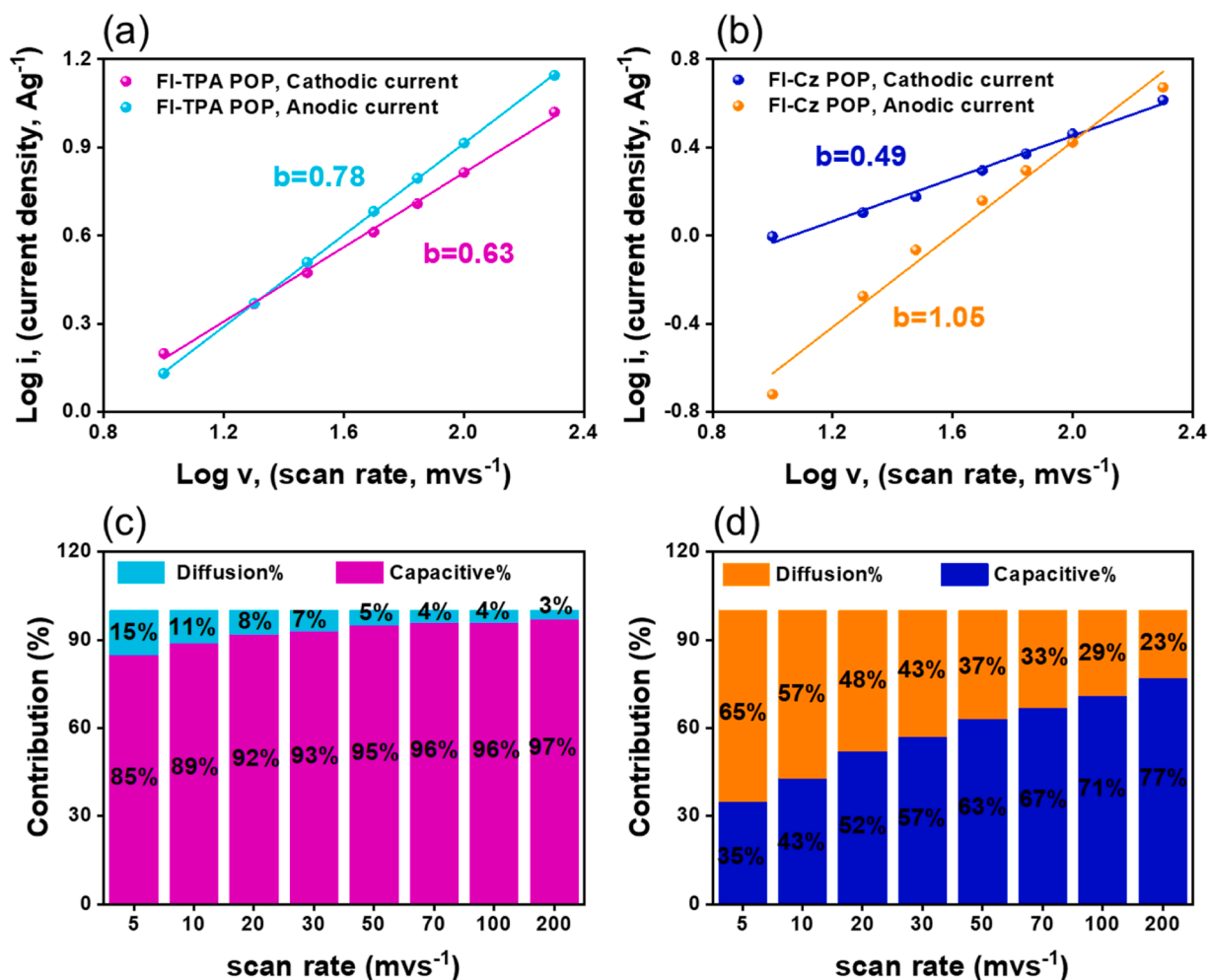


Fig. 6. (a and b) Log (*i*) against Log (*v*) curves of (a) FI-TPA, and (b) FI-Cz POPs. (c and d) The relative contributions of the capacitive and diffusion-controlled mechanisms of (c) FI-TPA, and (d) FI-Cz POPs, recorded at different scan rates.

Bode plots for the synthesized polymers. The calculated knee frequencies for the FI-TPA and FI-Cz POPs were found to be 82.54 Hz and 146.5 Hz, respectively, indicating their great potential for energy storage applications. (Figure S16b)

To gain a more comprehensive understanding of the capacitive contribution in the FI-TPA and FI-Cz POPs, the correlation between electrical current (*i*) and scan rate (*v*) was evaluated using the following equation [71].

$$i = av^b \quad (1)$$

By plotting log(*i*) against log(*v*), the resulting slope has been used to determine the value of “*b*,” while the value of “*a*” remains constant. The FI-TPA POP exhibited *b* values of 0.78 and 0.63 for the anodic and cathodic currents, respectively (Fig. 6a), whereas the FI-Cz POP displayed *b* values of 0.49 and 1.05 for the anodic and cathodic currents, respectively. (Fig. 6b)

The results obtained confirmed the presence of both capacitive and diffusion-controlled mechanisms in energy storage [72]. The remarkable capacitance rate of the FI-TPA POP was attributed to its greater capacitive contribution compared to that of the FI-Cz polymer. The capacitive and diffusion contributions relative to the total current can be calculated using the following equation: [71]

$$i(V) = k_1v + k_2v^{1/2} \quad (2)$$

At a constant scan rate *V*, the total current *i*(*V*) can be expressed as the sum of two components: $k_2v^{1/2}$, which represents the current arising

from diffusion-controlled processes, and k_1v , which accounts for the current due to capacitive mechanisms. For example, at a scan rate of 5 mV s^{-1} , the capacitive contributions of the FI-TPA and FI-Cz polymers were calculated to be 85 % and 35 % of their total capacity, respectively. By increasing the scan rate to 200 mV s^{-1} , the capacitive contribution of the FI-TPA POP rose to 97 % (Fig. 6c), while the FI-Cz polymer’s capacitive contribution increased to 77 %. (Fig. 6d) The relative contributions of capacitive and diffusion currents for the FI-based polymers recorded at 5 mV are shown in Figure S17.

4. Conclusions

In summary, two novel fluorene-based benzoxazine-linked POPs with exceptional thermal stability of up to $388 \text{ }^\circ\text{C}$ have been synthesized through a one-step Mannich coupling of triamino derivatives with 4,4’-(9H-fluorene-9,9-diyl)diphenol and paraformaldehyde. The heteroatom-enriched POPs demonstrated tunable porosities and favorable redox efficiency, rendering them effective electrodes for energy storage. Due to their hierarchical microporosity, excellent redox efficacy, and enhanced conductivity, the FI-TPA polymer achieved a maximum electrochemical capacitance of 276 F g^{-1} at a current density of 0.5 A g^{-1} and retained 95.23 % of its initial GCD capacitance over 5000 cycles at a current density of 10 A g^{-1} . Furthermore, the FI-TPA POP exhibited a notable energy density of 38.33 Wh kg^{-1} at a power density of 250 W kg^{-1} , along with a minimum resistance value of $21.83 \text{ } \Omega$. This current research may pave the way for new synthetic strategies,

enabling the exploration of innovative approaches for the preparation of heteroatom-rich POPs as promising candidates for energy storage applications.

Data availability

Data is contained within the article or Supplementary Material.

CRediT authorship contribution statement

Ahmed F. Saber: Writing – original draft, Investigation, Formal analysis, Data curation, Conceptualization. **Ahmed F.M. EL-Mahdy:** Writing – review & editing, Supervision. **Shiao-Wei Kuo:** Writing – review & editing, Supervision, Funding acquisition.

Declaration of competing interest

The authors declare that they have no known competing financial interests or personal relationships that could have appeared to influence the work reported in this paper.

Acknowledgements

This study was supported financially by the Ministry of Science and Technology, Taiwan, under contracts NSTC112–2218-E-110–007, 112–2223-E-110–002, 113-2218-E-110-004 and 112-2221-E-110-005-MY3.

Supplementary materials

Supplementary material associated with this article can be found, in the online version, at [doi:10.1016/j.jtice.2024.105935](https://doi.org/10.1016/j.jtice.2024.105935).

References

- Libich J, Máca J, Vondrák J, Čech O, Sedlářková M. Supercapacitors: properties and applications. *J Energy Storage* 2018;17:224–7.
- Wang SH, Li L, Wang H, Wang XW, Wang TH. Continuous and scalable manufacture of coal-derived hierarchical porous carbon dominated with mesopores for high rate-performance supercapacitors. *ACS Appl Energy Mater* 2024;7:4268–78.
- Yu Z, Tetard L, Zhai L, Thomas J. Supercapacitor electrode materials: nanostructures from 0 to 3 dimensions. *Energy Environ Sci* 2015;8:702–30.
- Samy MM, Mohamed MG, Mansoure TH, Meng TS, Khan MAR, Liaw CC, Kuo SW. Solid state chemical transformations through ring-opening polymerization of ferrocene-based conjugated microporous polymers in host-guest complexes with benzoxazine-linked cyclodextrin. *J Taiwan Inst Chem Eng* 2022;132:104110.
- Samy MM, Mohamed MG, Sharma SU, Chaganti SV, Lee JT, Kuo SW. An ultrastable tetrabenzonaphthalene-linked conjugated microporous polymer functioning as a high-performance electrode for supercapacitors. *J Taiwan Inst Chem Eng* 2024;158:104750.
- Saber AF, Sharma SU, Lee JT, EL-Mahdy AFM, Kuo SW. Carbazole-conjugated microporous polymers from Suzuki–Miyaura coupling for supercapacitors. *Polymer (Guildf)* 2022;254:125070–7.
- Zhao X, Sajjad M, Zheng Y, Zhao M, Li Z, Wu Z, Kang K, Qiu L. Covalent organic framework templated ordered nanoporous C60 as stable energy efficient supercapacitor electrode material. *Carbon N Y* 2021;182:144–54.
- Saber AF, Ahmed M, Kuo SW, EL-Mahdy AFM. Tetraphenylcyclopentadiene-based conjugated microporous polymers for high-performance energy storage carbons. *Polym Chem* 2023;14:4079–88.
- Zhao M, Zhao Q, Li B, Xue H, Pang H, Chen C. Recent progress in layered double hydroxide-based materials for electrochemical capacitors: design, synthesis and performance. *Nanoscale* 2017;9:15206–25.
- Winter M, Brodd RJ. What are batteries, fuel cells, and supercapacitors? *Chem Rev* 2004;104:4245–69.
- Zhang LL, Zhao XS. Carbon-based materials as supercapacitor electrodes. *Chem Soc Rev* 2009;38:2520–31.
- Mohamed MG, Atayde ECJ, Matsagar BM, Na J, Yamauchi Y, Wu KCW, Kuo SW. Construction hierarchically mesoporous/microporous materials based on block copolymer and covalent organic framework. *J Taiwan Inst Chem Eng* 2020;112:180.
- Xu L, Wang F, Ge X, Liu R, Xu M, Yang J. Covalent organic frameworks on reduced graphene oxide with enhanced electrochemical performance. *Microporous Mesoporous Mater* 2019;287:65–70.
- Saber AF, Kuo SW, EL-Mahdy AFM. Microporous carbons derived from nitrogen-rich triazatruxene-based porous organic polymers for efficient cathodic supercapacitors. *J Mater Chem A* 2024;12:15373.
- Geioushy RA, Attia SY, Mohamed SG, RA A, Fouad OA. Polyvinylpyrrolidone and freeze drying-assisted growth of an α -Ni(OH)₂/reduced graphene oxide hybrid structure as a superior electrode material for supercapacitors. *New J Chem* 2021;45:10012–20.
- Mei L, Cui X, Duan Q, Li Y, Lv X, Wang H. Metal phthalocyanine-linked conjugated microporous polymer hybridized with carbon nanotubes as a high-performance flexible electrode for supercapacitors. *Int J Hydrogen Energy* 2020;45:22950–8.
- Zhang T, Gregoriou VG, Gasparini N, Chochois CL. Porous organic polymers in solar cells. *Chem Soc Rev* 2022;51:4465–83.
- Zhang T, Xing G, Chen W, Chen L. Porous organic polymers: a promising platform for efficient photocatalysis. *Mater Chem Front* 2020;4:332–53.
- Tian L, Zhou S, Zhao J, Xu Q, Li N, Chen D, Li H, He J, Lu J. Sulfonate-modified calixarene-based porous organic polymers for electrostatic enhancement and efficient rapid removal of cationic dyes in water. *J Hazard Mater* 2023;441:129873.
- Xu C, Zhang W, Tang J, Pan C, Yu G. Porous organic polymers: an emerged platform for photocatalytic water splitting. *Front Chem* 2018;6:592.
- Luo D, Li M, Ma Q, Wen G, Dou H, Ren B, Liu Y, Wang X, Shui L, Chen Z. Porous organic polymers for Li-chemistry-based batteries: functionalities and characterization studies. *Chem Soc Rev* 2022;51:2917–38.
- Giri A, Khakre Y, Shreeraj G, Dutta TK, Kundu S, Patra A. The order–disorder conundrum: a trade-off between crystalline and amorphous porous organic polymers for task-specific applications. *J Mater Chem A* 2022;10:17077–121.
- Mphanje K. Polymeric nitrogen donor macro (meso) porous sorption materials for selected transition metals. University of Johannesburg, South Africa; 2015.
- Wang S, Li H, Huang H, Cao X, Chen X, Cao D. Porous organic polymers as a platform for sensing applications. *Chem Soc Rev* 2022;51:2031–80.
- Saber AF, Chen KY, EL-Mahdy AFM, Kuo SW. Designed azo-linked conjugated microporous polymers for CO₂ uptake and removal applications. *J Polym Res* 2021;28:1–12.
- Wang L, Su Y, Gu C. Solution processing of cross-linked porous organic polymers. *Acc Mater Res* 2022;3:1049–60.
- Mousa AO, Mohamed MG, Lin ZI, Chuang CH, Chen CK, Kuo SW. Construction of cationic conjugated microporous polymers containing pyrene units through post-cationic modification for enhanced antibacterial performance. *J Taiwan Inst Chem Eng* 2024;157:105448.
- Huang L, Miao J, Shuai Q. Carboxyl-functionalized magnetic porous organic polymers as efficient adsorbent for wastewater remediation. *J Taiwan Inst Chem Eng* 2020;109:97.
- Yang CH, Chang JS, Lee DJ. Chemically stable covalent organic framework as adsorbent from aqueous solution: a mini-review. *J Taiwan Inst Chem Eng* 2020;110:79.
- Saber AF, EL-Mahdy AFM. E)-1,2-Diphenylethene-based conjugated nanoporous polymers for a superior adsorptive removal of dyes from water. *New J Chem* 2021;45:21834–43.
- Giri L, Rout SR, Varma RS, Otyepka M, Jayaramulu K, Dandela R. Recent advancements in metal–organic frameworks integrating quantum dots (QDs@MOF) and their potential applications. *Nanotechnol Rev* 2022;11:1947–76.
- Saber AF, Elewa AM, Chou HH, EL-Mahdy AFM. Donor-acceptor carbazole-based conjugated microporous polymers as photocatalysts for visible-light-driven H₂ and O₂ evolution from water splitting. *Appl Catal B* 2022;316:121624.
- Rajagopal V, Kathiresan M, Manivel P, Suryanarayanan V, Velayutham D, Ho KC. Porous organic polymer derived metal-free carbon composite as an electrocatalyst for CO₂ reduction and water splitting. *J Taiwan Inst Chem Eng* 2020;106:183.
- Liu X, Liu CF, Xu S, Cheng T, Wang S, Lai WY, Huang W. Porous organic polymers for high-performance supercapacitors. *Chem Soc Rev* 2022;51:3181–225.
- Saber AF, Elewa AM, Chou HH, EL-Mahdy AFM. Donor to acceptor charge transfer in carbazole-based conjugated microporous polymers for enhanced visible-light-driven photocatalytic water splitting. *ChemCatChem* 2023;15:e202201287.
- Saber AF, Chueh CC, Rashad M, Kuo SW, EL-Mahdy AFM. Thiazolyl-linked conjugated microporous polymers for enhancement adsorption and photocatalytic degradation of organic dyes from water. *Mater Today Sustain* 2023;23:100429.
- Yuan S, Kirklın S, Dorney B, Liu DJ, Yu L. Nanoporous polymers containing stereocontorted cores for hydrogen storage. *Macromolecules* 2009;42:1554–9.
- Paraknowitsch JP, Thomas A. Doping carbons beyond nitrogen: an overview of advanced heteroatom doped carbons with boron, sulphur and phosphorus for energy applications. *Energy Environ Sci* 2013;6:2839–55.
- Wood KN, O'Hayre R, Pilypenko S. Recent progress on nitrogen/carbon structures designed for use in energy and sustainability applications. *Energy Environ Sci* 2014;7:1212–49.
- Arslan M, Kiskan B, Yagci Y. Benzoxazine-Based Thermosets with Autonomous Self-Healing Ability. *Macromolecules* 2015;48:1329–34.
- Mahfud R, Agag T, Ishida H, Shaikh S, Qutubuddin S. Synthesis and evaluation of novel anionic polymeric surfactants based on polybenzoxazines. *J Colloid Interface Sci* 2013;407:339–47.
- Choi SW, Park JO, Pak C, Choi KH, Lee JC, Chang H. Design and synthesis of cross-linked copolymer membranes based on poly(benzoxazine) and polybenzimidazole and their application to an electrolyte membrane for a high-temperature PEM fuel cell. *Polymers (Basel)* 2013;5:77–111.
- Alhassan SM, Qutubuddin S, Schiraldi DA, Agag T, Ishida H. Preparation and thermal properties of graphene oxide/main chain benzoxazine polymer. *Eur Polym J* 2013;49:3825–33.

- [44] Liu J, Ishida H. Anomalous isomeric effect on the properties of bisphenol f-based benzoxazines: toward the molecular design for higher performance. *Macromolecules* 2014;47:5682–90.
- [45] Thubsuang U, Ishida H, Wongkasemjit S, Chaisuwan T. Improvement in the pore structure of polybenzoxazine-based carbon xerogels through a silica templating method. *J Porous Mater* 2014;21:401–11.
- [46] Wan L, Wang J, Feng C, Sun Y, Li K. Synthesis of polybenzoxazine based nitrogen-rich porous carbons for carbon dioxide capture. *Nanoscale* 2015;7:6534–44.
- [47] Taskin OS, Kiskan B, Aksu A, Balkis N, Weber J, Yagci Y. Polybenzoxazine: a powerful tool for removal of mercury salts from water. *Chem Eur J* 2014;20:10953–8.
- [48] Wang S, Zhang L, Han F, Li WC, Xu YY, Qu WH, Lu AH. Diaminohexane-assisted preparation of coral-like, poly(benzoxazine)-based porous carbons for electrochemical energy storage. *ACS Appl Mater Interfaces* 2014;6:11101–9.
- [49] Sevilla M, Fuertes AB. Fabrication of porous carbon monoliths with a graphitic framework. *Carbon N Y* 2013;56:155–66.
- [50] Xu S, He J, Jin S, Tan B. Heteroatom-rich porous organic polymers constructed by benzoxazine linkage with high carbon dioxide adsorption affinity. *J Colloid Interface Sci* 2018;509:457–62.
- [51] Kim Y, Lim E. Development of polymer acceptors for organic photovoltaic cells. *Polymers (Basel)* 2014;6:382–407.
- [52] Carbas BB. Fluorene based electrochromic conjugated polymers: a review. *Polymer (Guildf)* 2022;254:125040.
- [53] Wallace JU, Chen SH. Fluorene-based conjugated oligomers for organic photonics and electronics. *Adv Polym Sci* 2008;212:145–86.
- [54] Xu PY, Zhou K, Han GL, Zhang QG, Zhu AM, Liu QL. Effect of fluorene groups on the properties of multiblock poly(Arylene Ether Sulfone)s-based anion-exchange membranes. *ACS Appl Mater Interfaces* 2014;6:6776–85.
- [55] Baczkowski ML, Wang DH, Lee DH, Lee KM, Smith ML, White TJ, Tan LS. Photomechanical deformation of azobenzene-functionalized polyimides synthesized with bulky substituents. *ACS Macro Lett* 2017;6:1432–7.
- [56] Sun W, Zhou N, Xiao Y, Wang S, Li X. Novel carbazolyl-substituted spiro[acridine-9,9'-fluorene] derivatives as deep-blue emitting materials for OLED applications. *Dyes Pigm* 2018;154:30–7.
- [57] Yanping H, Xiaoming F, Baohua H, Kun Z, Xiaoli N, Heping Z. New progress of researches in fluorene compounds. *Chin J Org Chem* 2012;32:1169–85.
- [58] Xie LH, Yang SH, Lin JY, Yi MD, Huang W. Fluorene-based macromolecular nanostructures and nanomaterials for organic (opto)electronics. *Phil Trans R Soc A* 2013;371:e20120337.
- [59] Mahfud R, Agag T, Ishida H, Shaikh S, Qutubuddin S. Synthesis and evaluation of novel anionic polymeric surfactants based on polybenzoxazines. *J Colloid Interface Sci* 2013;407:339–47.
- [60] Zhou C, Lu X, Xin Z, Liu J, Zhang Y. Hydrophobic benzoxazine-cured epoxy coatings for corrosion protection. *Prog Org Coat* 2013;76:1178–83.
- [61] Takeichi T, Thongpradith S, Kawauchi T. Copolymers of vinyl-containing benzoxazine with vinyl monomers as precursors for high performance thermosets. *Molecules* 2015;20:6488–503.
- [62] Mohamed MG, Chen TC, Kuo SW. Solid-State chemical transformations to enhance gas capture in benzoxazine-linked conjugated microporous polymers. *Macromolecules* 2021;54:5866–77.
- [63] Ejaz M, Mohamed MG, Kuo SW. Solid state chemical transformation provides a fully benzoxazine-linked porous organic polymer displaying enhanced CO₂ capture and supercapacitor performance. *Polym Chem* 2023;14:2494.
- [64] Lee JSM, Cooper AI. Advances in conjugated microporous polymers. *Chem Rev* 2020;120:2171–214.
- [65] Sheng Q, Zhong X, Shang Q, Dong YY, Zhao J, Du Y, Xie Y. Triazine-based conjugated microporous polymers with different linkage units for visible light-driven hydrogen evolution. *Front Chem* 2022;10:854018.
- [66] Aitchison CM, Sprick RS, Cooper AI. Emulsion polymerization derived organic photocatalysts for improved light-driven hydrogen evolution. *J Mater Chem A* 2019;7:2490–6.
- [67] Mohamed MG, Elewa AM, Li MS, Kuo SW. Construction and multifunctional of hyper-crosslinked porous organic polymers containing ferrocene unit for high-performance iodine adsorption and supercapacitor. *J Taiwan Inst Chem Eng* 2023;150:105045.
- [68] Mei L, Cui X, Duan Q, Li Y, Lv X, Wang HG. Metal phthalocyanine-linked conjugated microporous polymer hybridized with carbon nanotubes as a high-performance flexible electrode for supercapacitors. *Int J Hydrogen Energy* 2020;45:22950–8.
- [69] Khattak AM, Ghazi ZA, Liang B, Khan NA, Iqbal A, Li L, Tang Z. A redox-active 2D covalent organic frameworks with pyridine moieties capable of faradic energy storage. *J Mater Chem A* 2016;4:16312–7.
- [70] Xu Q, Tang Y, Zhai L, Chen Q, Jiang D. Pyrolysis of covalent organic frameworks: a general strategy for template converting conventional skeletons into conducting microporous carbons for high-performance energy storage. *Chem Commun* 2017;53:11690–3.
- [71] Li Q, Lu W, Li Z, Ning J, Zhong Y, Hu Y. Hierarchical MoS₂/NiCo₂S₄@C urchin-like hollow microspheres for asymmetric supercapacitors. *Chem Eng J* 2020;380:122544.
- [72] Lim E, Jo C, Kim H, Kim MH, Mun Y, Chun J, Ye Y, Hwang J, Ha KS, Roh KC, Kang K, Yoon S, Lee J. Facile synthesis of Nb₂O₅@Carbon core-shell nanocrystals with controlled crystalline structure for high-power anodes in hybrid supercapacitors. *ACS Nano* 2015;9:7497–505.